

# Fabrication of Nanoporous Nickel–Iron Hydroxylphosphate Composite as Bifunctional and Reversible Catalyst for Highly Efficient Intermittent Water Splitting

Zhanwu Lei,<sup>†</sup> Jingjing Bai,<sup>†</sup> Yibing Li,<sup>‡</sup><sup>✉</sup> Zenglin Wang,<sup>\*,†</sup><sup>✉</sup> and Chuan Zhao<sup>\*,†,‡</sup><sup>✉</sup>

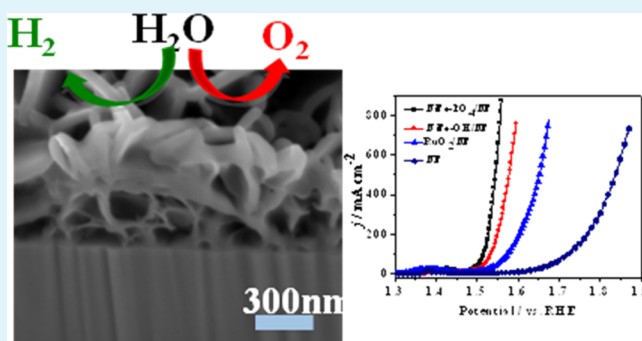
<sup>†</sup>Key Laboratory of Applied Surface and Colloid Chemistry, Ministry of Education, School of Chemistry and Chemical Engineering, Shaanxi Normal University, Xi'an 710062, China

<sup>‡</sup>School of Chemistry, The University of New South Wales, Sydney, NSW 2052, Australia

## Supporting Information

**ABSTRACT:** Global-scale application of water-splitting technology for hydrogen fuel production and storage of intermittent renewable energy sources has called for the development of oxygen- and hydrogen-evolution catalysts that are inexpensive, efficient, robust, and can withstand frequent power interruptions and shutdowns. Here, we report the controlled electrodeposition of porous nickel–iron hydroxylphosphate ( $\text{NiFe-OH-PO}_4$ ) nanobelts onto the surface of macroporous nickel foams (NF) as a bifunctional electrocatalyst for efficient whole-cell water electrolysis. The  $\text{NiFe-OH-PO}_4/\text{NF}$  electrode shows both high water oxidation and water reduction catalytic activity in alkaline solutions and is able to deliver current densities of 20 and 800  $\text{mA cm}^{-2}$  at overpotentials of merely 249 and 326 mV for oxygen-evolution reaction, current densities of 20 and 300  $\text{mA cm}^{-2}$  at overpotentials of only 135 and 208 mV for hydrogen-evolution reaction. Further, in a two-electrode water electrolytic cell, the bifunctional  $\text{NiFe-OH-PO}_4/\text{NF}$  electrodes can obtain the current densities of 20 and 100  $\text{mA cm}^{-2}$  at an overall cell potential of only 1.68 and 1.91 V, respectively. Remarkably, the  $\text{NiFe-OH-PO}_4/\text{NF}$  catalyst also represents prolonged stability under both continuous and intermittent electrolysis and can be used for oxygen evolution and hydrogen evolution reversibly without degradation.

**KEYWORDS:** NiFe hydroxylphosphate composite, water reduction and water oxidation, electrocatalysis, intermittent electrolysis, bifunctional catalyst



## INTRODUCTION

Hydrogen, as a clean and renewable energy carrier, has been intensely investigated as an alternative to fossil fuels.<sup>1,2</sup> Water electrolysis offers an effective way to make high-purity hydrogen; however, its practical use for mass production of hydrogen is limited owing to high energy consumption.<sup>3</sup> Active electrocatalysts for the anodic oxygen-evolution reaction (OER) and the cathodic hydrogen-evolution reaction (HER) are required to overcome the large overpotentials and to make the process more energy efficient.<sup>4–7</sup> Significant progress has been achieved during the past few years in developing nonprecious metal catalysts with high activity for OER such as oxides,<sup>8</sup> hydroxides,<sup>9</sup> phosphate,<sup>10</sup> chalcogenides,<sup>11</sup> nickel-based materials<sup>12,13</sup> and for HER such as phosphide,<sup>14</sup> phosphate,<sup>15</sup> carbide,<sup>16</sup> oxides,<sup>17</sup> and chalcogenides.<sup>18</sup> On the other hand, recently, steels have also shown high activity as a renaissance water-splitting catalyst.<sup>19–24</sup>

Recent studies have reported the use of bifunctional catalysts for overall water splitting; these catalysts can potentially remove the problems associated with catalyst contamination and

membrane separators, thus improving the integration and simplification of the water-splitting system and lowering the manufacturing cost of the produced hydrogen. Furthermore, for practical applications, the catalysts also must withstand frequent cell shutdowns, when the electrodes can be depolarized and are susceptible to corrosion owing to the reversed current.<sup>25,26</sup> This is very important for the storage of electricity generated from renewable resources such as solar and wind energy because these energy sources are intermittent and power interruptions are almost inevitable. However, the design of bifunctional electrodes that are active and stable toward both OER and HER in the same electrolytes (either strongly acidic or strongly alkaline) and can withstand frequent power shutdowns while maintaining high activity and stability still remains a challenge for most of earth-abundant materials.

Received: July 17, 2017

Accepted: October 2, 2017

Published: October 2, 2017

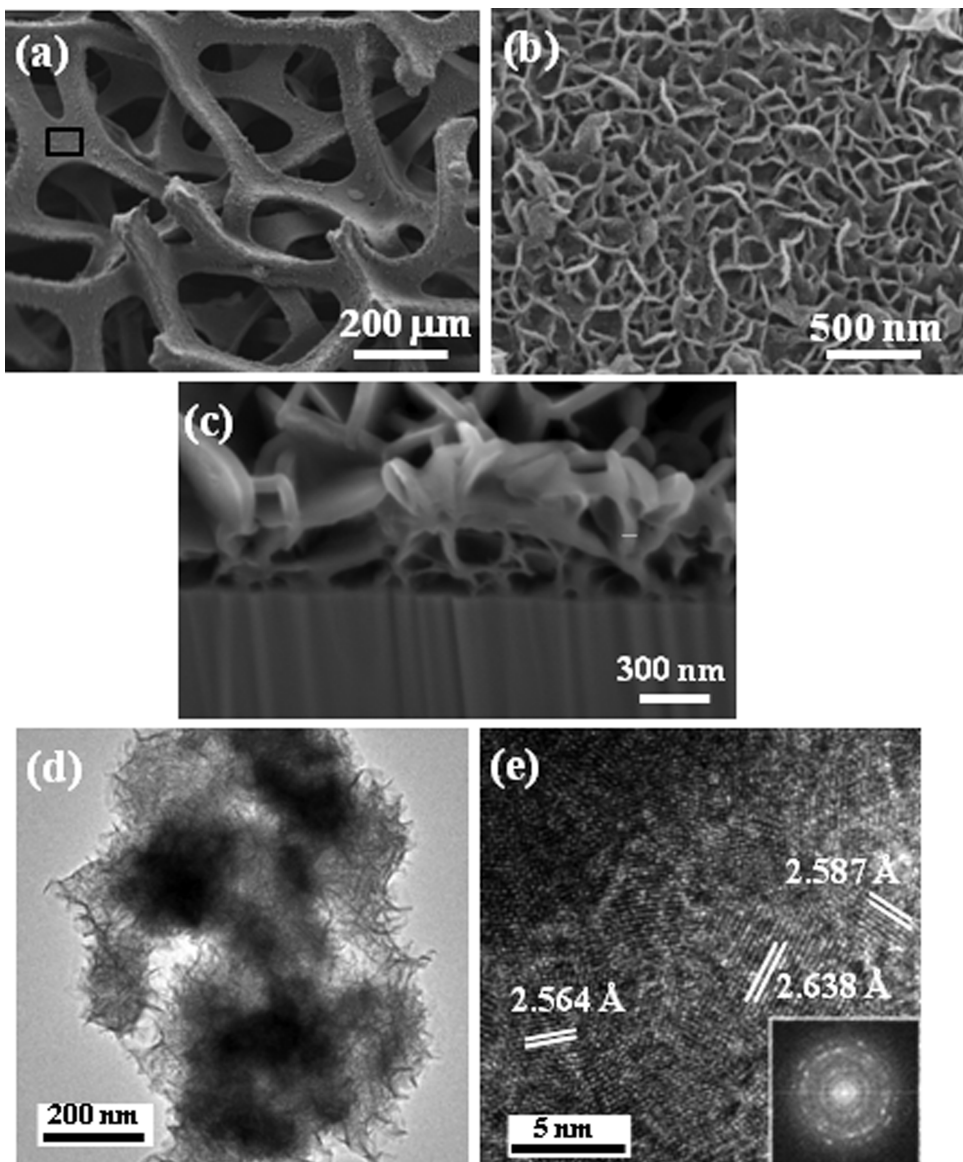


**Figure 1.** (a) SEM image of NiFe-OH-PO<sub>4</sub>/NF. (b) SEM image of the square marked in (a) under high magnifications. (c) FIB cross-sectional SEM image of NiFe-OH-PO<sub>4</sub>/NF. (d) TEM image and (e) high-resolution transmission electron microscopy (HR-TEM) image of NiFe-OH-PO<sub>4</sub> nanobelt sample.

To meet these harsh conditions for industrial water electrolysis, it is fundamental to develop cost-effective, robust, highly active water-splitting electrode materials that can be easily mass produced at low cost. Our recent studies have demonstrated that porous nickel–iron hydroxide (dubbed NiFe-OH), as a promising OER catalyst, exhibits extraordinary catalytic activity and stability in an alkaline solution.<sup>27</sup> Some studies also have shown remarkable catalytic properties of transitional metal based phosphide/phosphate<sup>28</sup> for HER and OER. Further, Ng et al. reported a highly efficient bifunctional electrocatalyst of nickel–iron phosphates (dubbed NiFe-PO<sub>4</sub>) on a three-dimensional (3D) nickel foam (NF) via a cyclic voltammetry (CV) approach for water splitting.<sup>29</sup> This inspires us to develop a bifunctional NiFe-based hydroxide phosphate for both OER and HER. However, it is technically difficult to combine these two transitional metal compounds in one system in a controllable manner because the metal hydroxide compounds are usually prepared in a chemical reduction

environment, whereas the formation of the phosphate groups usually requires an oxidation environment.

In this study, we present a facile cyclic voltammetry method for the controlled electrodeposition preparation of novel bifunctional water-splitting nickel–iron hydroxyphosphate electrocatalyst (dubbed NiFe-OH-PO<sub>4</sub>) composed of a synergistic NiFe hydroxide and NiFe phosphate phase structure. In the electrolyte bath containing Ni<sup>2+</sup>, Fe<sup>2+</sup>, and H<sub>2</sub>PO<sub>4</sub><sup>-</sup>, cathodic potential sweeps generate OH<sup>-</sup> to form NiFe hydroxide, which are subsequently phosphorylated on the anodic sweeps via the oxidation of hypophosphite groups. Repetitive potential cycles lead to the deposition of nanoporous NiFe-OH-PO<sub>4</sub> nanobelts with tunable composition, structure, and electrocatalytic properties on the nickel foams (NF) substrate. The NiFe-OH-PO<sub>4</sub>/NF catalyst exhibits extraordinary high OER and HER activities at low electrocatalytic overpotentials. Remarkably, employed as both anode and cathode electrode in a two-electrode water electrolysis cell, the

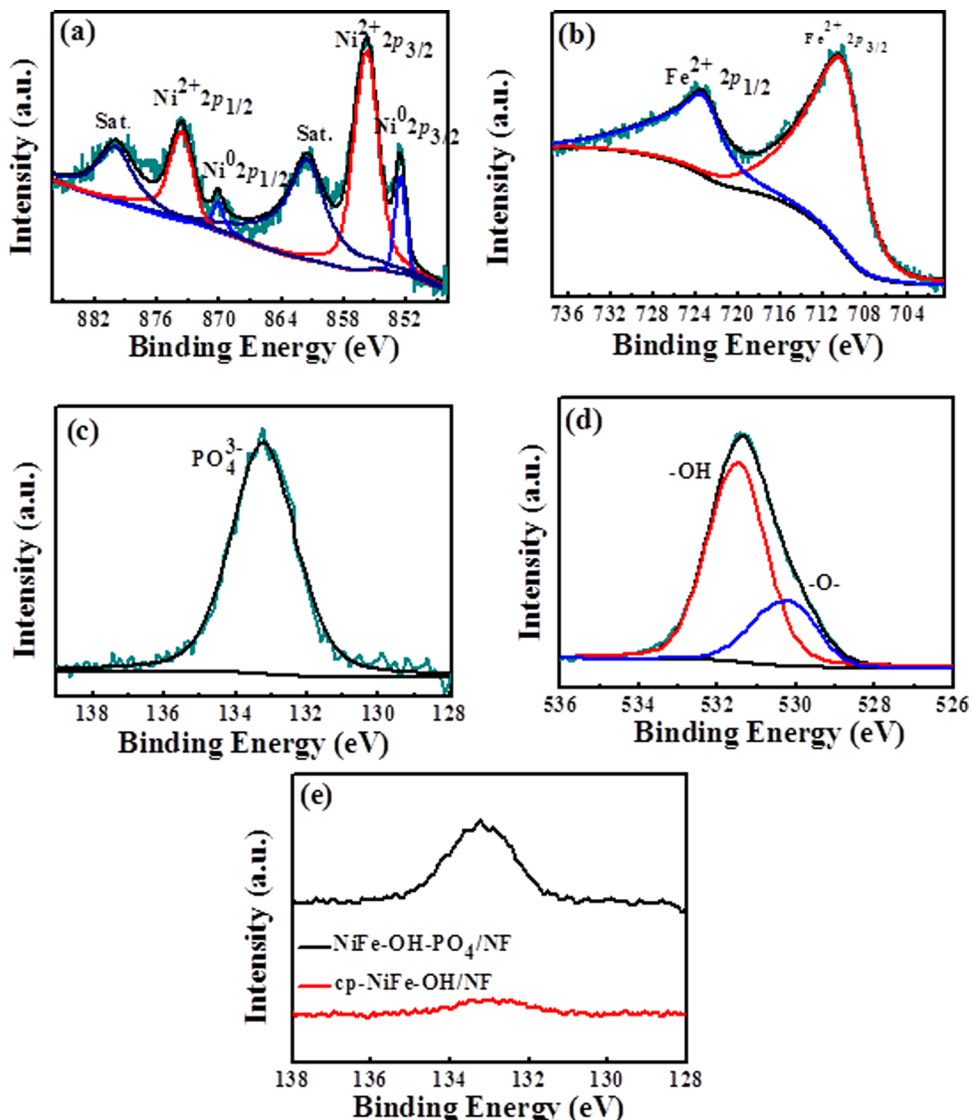


**Figure 2.** X-ray photoelectron spectra of NiFe-OH-PO<sub>4</sub>/NF: (a) Ni 2p, (b) Fe 2p, (c) P 2p, (d) O 1s, and (e) P 2p of NiFe-PO<sub>4</sub>/NF and cp-NiFe-OH /NF.

bifunctional NiFe-OH-PO<sub>4</sub>/NF electrode exhibits prolonged stability under both continuous and intermittent electrolysis.

## EXPERIMENTAL SECTION

**Fabrication of Nickel–Iron Hydroxide (NiFe-OH) and Nickel–Iron Hydroxylphosphate (NiFe-OH-PO<sub>4</sub>) Nanobelts on NF.** Nickel foam (NF) ( $2.0 \times 0.5 \times 0.05$  cm $^3$ ) was pretreated in 5.0 M HCl acid solution at ambient temperature for 20 min to remove the oxidized NiO layer from the NF surface before starting electrodeposition. The NiFe-OH-PO<sub>4</sub> was then electrodeposited onto the NF by cyclic voltammetry (CV) approach in a solution with 3.0 mM NiCl<sub>2</sub>·6H<sub>2</sub>O, 3.0 mM FeCl<sub>2</sub>·4H<sub>2</sub>O, and 1.0 mM NaH<sub>2</sub>PO<sub>4</sub>. The electrodeposition was carried out in a three-electrode cell using NF as the working electrode, a graphite rod as the counter electrode, and Ag/AgCl (sat. KCl) as the reference electrode at a scan rate of 5.0 mV·s $^{-1}$  in the potential ranging from 0.20 to −1.20 V for eight cycles, which is different from that of NiFe-PO<sub>4</sub> composite.<sup>29</sup> NiFe-OH was electrodeposited on NF following the same procedure, except without using NaH<sub>2</sub>PO<sub>4</sub>. After that, the as-prepared NiFe-OH-PO<sub>4</sub>/NF and NiFe-OH/NF were cleaned with ethanol and distilled water and then dried in vacuum.

**Preparation of RuO<sub>2</sub>/NF Electrode.** The method of preparation of the RuO<sub>2</sub>/NF electrode was the same as that reported previously.<sup>27</sup>

**Materials Characterization.** The as-deposited NiFe-OH-PO<sub>4</sub>/NF nanobelts were characterized by X-ray diffraction (XRD, Rigaku D/MAX 2550, Japan), field emission scanning electron microscopy (FEI Nova Nano SEM 450), X-ray photoelectron spectroscopy (XPS, AXIS ULTRA XPS system), transmission electron microscopy (TEM), and energy-dispersive X-ray spectroscopy mappings (Tecnai G2 F20 TEM instrument). To prepare the samples for cross-sectional scanning electron microscopy (SEM), the NiFe-OH-PO<sub>4</sub>/NF electrodes were cut by a focused ion beam (FIB). To prevent the surface from etching during the FIB process, a carbon layer few tens of nanometers thick was evaporated on the sample surface. Raman spectroscopy was performed using a laser micro-Raman spectrometer (Renishaw) by employing a laser with an incident wavelength of 532 nm.

**Electrochemical Characterization.** All of the electrochemical measurements were carried out with a CHI660D electrochemical workstation in 1.0 M KOH electrolyte solution. The as-prepared NiFe-OH-PO<sub>4</sub>/NFs were used directly as the working electrode without further treatments. The electrochemical characterizations were carried in a standard three-electrode system by using a graphite rod counter electrode and a Ag/AgCl (sat. KCl) reference electrode. All of the potentials measured were converted to reversible hydrogen electrode (RHE) using the following equation:  $E_{\text{RHE}} = E_{\text{Ag/AgCl}} + 0.197 \text{ V} + 0.059 \text{ pH}$ . Unless otherwise stated, OER and HER polarization curves are recorded at a scan rate of 2.0 mV s $^{-1}$  with 95%  $iR$  compensation.

The  $iR$  compensations were determined automatically using the potentiostat. Chronopotentiometric and chronoampermetric measurements are obtained under the same experimental conditions without compensating for the  $iR$  drop. Electrochemical impedance spectra (EIS) of the samples were recorded at 1.53 V (vs RHE) for OER and at −0.15 V for HER in the frequency range of 0.1–10<sup>5</sup> Hz with an AC voltage of 5 mV in 1 M KOH electrolyte. The turnover frequency (TOF) values of NiFe-OH-PO<sub>4</sub>/NFs electrodes are calculated according to the following equation.<sup>27</sup>

$$\text{TOF} = JA/(4Fn)$$

where  $J$  is the current density at the overpotential of 300 mV,  $A$  is the area of the NiFe-OH-PO<sub>4</sub>/NF electrode,  $F$  is the Faraday constant (a value of 96 485 C mol<sup>−1</sup>), and  $n$  is the number of moles of the active materials deposited onto the nickel foams. The electrochemically active surface areas (ECAS) of the samples were estimated by double-layer capacitance measurements.<sup>27</sup>

## RESULTS AND DISCUSSION

**Sample Synthesis and Characterization.** Nickel–iron hydroxyphosphate (NiFe-OH-PO<sub>4</sub>) composite was electrodeposited onto the NF by eight cyclic voltammetry (CV) cycles in an electrolyte solution containing 3.0 mM NiCl<sub>2</sub>, 3.0 mM FeCl<sub>2</sub>, and 1.0 mM NaH<sub>2</sub>PO<sub>2</sub> in the potential range of −1.2 to 0.2 V (vs Ag/AgCl). When the potential was scanned to negative direction, water on the surface of the working electrode began to be reduced to form OH<sup>−</sup> ions (at potential of ~0.8 V in pure water; Figure S1a). Then, the generated OH<sup>−</sup> ions reacted with Ni<sup>2+</sup> and Fe<sup>2+</sup> form NiFe hydroxide precipitates at the electrode surface (Figure S1b,c). The subsequent positive potential direction scan caused the oxidation of hypophosphite ions (at potential of 0 V, Figure S1d), finally leading to the formation of NiFe hydroxyphosphate composites. Overall, the formation of NiFe hydroxyphosphate can be described through the following reaction (eq 1)

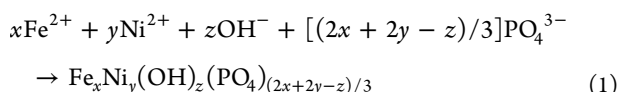


Figure 1a shows the low-magnification SEM image of NiFe-OH-PO<sub>4</sub>/NF, indicating that the composite was uniformly coated on the NF surface. The high-magnification SEM image reveals that NiFe-OH-PO<sub>4</sub> nanobelts having a length of 200–300 nm and a thickness of 40–70 nm are assembled vertically on the NF with a three-dimensional porous structure (Figure 1b). The FIB cross-sectional SEM image (Figure 1c) demonstrates that the porous NiFe-OH-PO<sub>4</sub> film possesses a thickness of around 500 nm, with various interconnected channels between 50 and 500 nm. This morphology can not only increase the specific surface area of the catalyst but also provide pathways for a fast mass transport and dissipation of gaseous products. Interestingly, it is noted that the size of nanobelts on the outer layers of the porous film is larger than those in the inner layers (Figure 1c), suggesting that the deposition rate of the NiFe-OH-PO<sub>4</sub> composite is faster at the outer surface. However, little change in the deposited film thickness was found with increase in number of the deposition cycles. As seen in Figure S2a, after only 1 CV deposition cycle, many nanobelts with a length of ~100 nm are already deposited onto the NF surface to form porous films. With an increment in the number of deposition cycles, the morphology change is small, but the nanobelts appear to become thicker and larger (Figure S2b,c). After eight deposition cycles, an

optimal nanoporous film with interconnected nanobelts is successfully generated.

The porous nanobelt morphology of the NiFe-OH-PO<sub>4</sub> scratched off from the NF surface is also studied by transmission electron microscopy (TEM), as shown in Figure 1d. The NiFe-OH-PO<sub>4</sub> composite shows a nanobelt structure, which is in good agreement with the SEM result. The HR-TEM image of the NiFe-OH-PO<sub>4</sub> nanobelts displays well-resolved lattice fringes (Figure 1e), with an average lattice distance of ~0.26 nm. The scanning transmission electron microscopy image and the elemental mapping performed on NiFe-OH-PO<sub>4</sub> reveals that Ni, Fe, P, and O elements are uniformly distributed over the entire film (Figure S3).

The X-ray photoelectron spectroscopy (XPS) of NiFe-OH-PO<sub>4</sub> composite showed all of the anticipated elements (Figure S4). In the high-resolution Ni 2p spectrum (Figure 2a), the two peaks centered at 873.5 and 855.7 eV, accompanied by two satellite peaks corresponding to Ni 2p<sub>3/2</sub> and Ni 2p<sub>1/2</sub> binding energies,<sup>30</sup> match well with that of nickel(II) hydroxide.<sup>31</sup> The peaks of Ni 2p at 870.1 and 852.5 eV are assigned to metal nickel of NF.<sup>32</sup> The two peaks appearing at Fe 2p at 723.3 and 710.2 eV (Figure 2b), corresponding to Fe 2p<sub>3/2</sub> and Fe 2p<sub>1/2</sub>, are assigned to iron(II) hydroxide.<sup>33</sup> The binding energy of P 2p shows a sole peak centered at ~133.2 eV (Figure 2c), indicating the formation of phosphate bond.<sup>34</sup> The formation of NiFe-OH-PO<sub>4</sub> is also demonstrated by the high-resolution O 1s XPS spectra that can be deconvoluted into two peaks (Figure 2d). The peaks at ~530.9 and ~529.6 eV are ascribed to the hydroxyl group and the surface-adsorbed oxygen, respectively.<sup>35,36</sup> Taken together, all of the above experimental data suggest that NiFe hydroxyphosphate composite is successfully electrodeposited on the NF substrate, and the mole ratio of Ni, Fe, and P in the NiFe-OH-PO<sub>4</sub> composite is determined to be 1:1:0.3.

To confirm the formation mechanism of NiFe-OH-PO<sub>4</sub> via cyclic voltammetry (eq 1), constant potential electrodeposition was carried out at −1.2 V versus Ag/AgCl for 5 min, without the subsequent anodic phosphorylation. The obtained sample (denoted as cp-NiFe-OH/NF) was also investigated by XPS. As seen in Figure 2e, no significant peak is observed for P 2p, except very weak signal attributed to the physically adsorbed H<sub>2</sub>PO<sub>2</sub><sup>−</sup> from the electrolytes. These results confirm that the oxidation of H<sub>2</sub>PO<sub>2</sub><sup>−</sup> to PO<sub>4</sub><sup>3−</sup> at the anodic scans is essential for the formation of the NiFe-OH-PO<sub>4</sub> composites. As a result, the cp-NiFe-OH/NF exhibits a much lower catalytic activity than the NiFe-PO<sub>4</sub>/NF composite (see below).

Raman spectroscopy was also used to characterize the structure of the electrodeposited composite (Figure S5). Three peaks of NiFe-OH composite at 327, 453, and 534 cm<sup>−1</sup> are ascribed to typical vibration peaks of Fe–O,<sup>37</sup> the symmetric Ni–OH stretching, and the Ni–O stretching mode, respectively.<sup>38</sup> A new peak of NiFe-OH-PO<sub>4</sub> at 685 cm<sup>−1</sup> is ascribed to P–O vibration peaks, which once again confirms the formation of the synergistic NiFe hydroxyphosphate structure by the facile electrodeposition route.<sup>39</sup>

The XRD of NiFe-PO<sub>4</sub>/NF only shows three diffraction peaks at 44.5, 51.8, and 76.4° (Figure S6) that are attributed to the nickel (111), (200), and (220) diffraction peaks from the NF.<sup>39</sup> No characteristic diffraction peak belonging to NiFe-OH-PO<sub>4</sub> hydroxide composite is observed, suggesting the as-deposited NiFe-OH-PO<sub>4</sub> composite is amorphous in nature. Combination of the HR-TEM results suggests that the as-

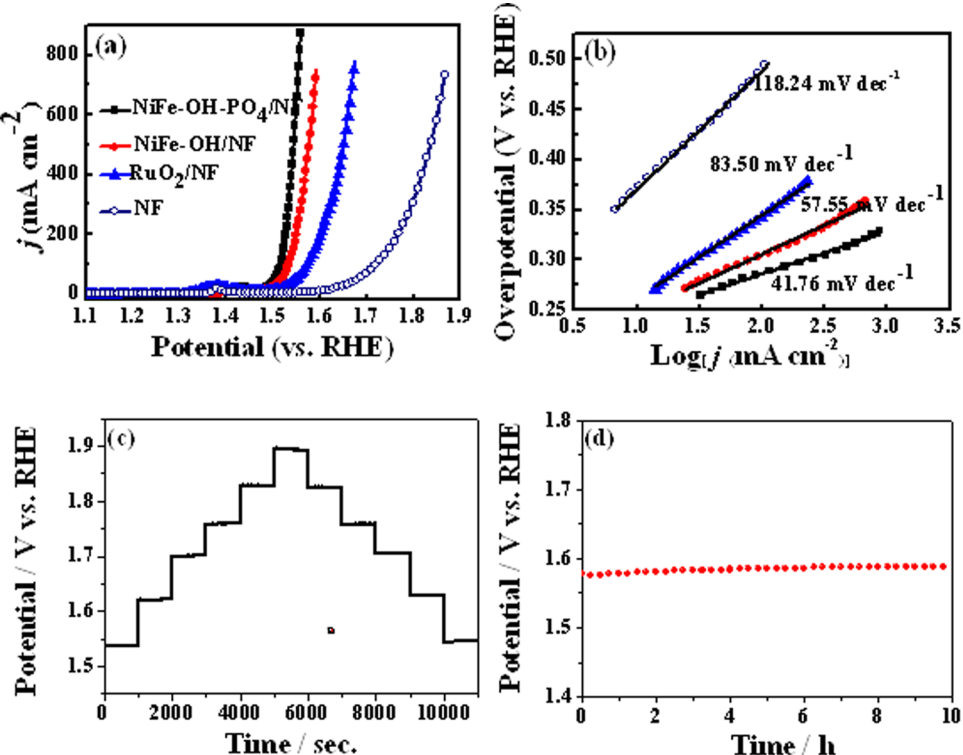


**Figure 3.** (a) OER polarization curves for NiFe-OH-PO<sub>4</sub>/NF, NiFe-OH/NF, RuO<sub>2</sub>/NF, and NF electrodes at 2.0 mV s<sup>-1</sup> with  $iR$  compensations. (b) The corresponding Tafel plots. (c) Multicurrent process of NiFe-OH-PO<sub>4</sub>/NF. The current density started at 50 and ended at 550 mA cm<sup>-2</sup> with an increment of 100 mA cm<sup>-2</sup> per 1000 s. (d) Chronopotentiometric curve of NiFe-OH-PO<sub>4</sub>/NF with constant current density of 100 mA cm<sup>-2</sup>. All of the experiments were carried out in 1.0 M KOH.

deposited NiFe-OH-PO<sub>4</sub> composite possesses both short-range order and long-range disordered structure.

**Oxygen Evolution Activity.** The electrocatalytic performances for OER of the NiFe-OH-PO<sub>4</sub>/NF electrode in O<sub>2</sub>-saturated 1.0 M KOH solution are firstly investigated. As a comparison, electrodeposited NiFe-OH/NF, commercial RuO<sub>2</sub> powder dispersed on NF (RuO<sub>2</sub>/NF), and NF electrode were also investigated, and the results are shown in Figure 3a. The NiFe-OH/NF electrode exhibits an overpotential ( $\eta$ ) of 264 mV at a current density of 20 mA cm<sup>-2</sup> (Figure 3a), which is much lower than the value obtained for RuO<sub>2</sub>/NF electrode (288 mV). In contrast, the NiFe-PO<sub>4</sub>/NF electrode required merely  $\eta = 249$  mV to deliver a current density of 20 mA cm<sup>-2</sup>, suggesting a significant improvement in its OER activity after phosphorylation. The overpotential value is the lowest among the state-of-the-art bifunctional electrocatalysts for OER under similar conditions, including CoO<sub>x</sub>@CN (260 mV),<sup>40</sup> NiFe-LDH/NF (269 mV),<sup>41</sup> Ni<sub>3</sub>S<sub>2</sub> /NF (260 mV),<sup>42</sup> CoP-MNA (290 mV),<sup>43</sup> PCPTF (330 mV),<sup>44</sup> and Ni<sub>5</sub>P<sub>4</sub> (290 mV)<sup>45</sup> (Table S1). Moreover, for a high current density of 800 mA cm<sup>-2</sup>, only a small  $\eta = 326$  mV is required for NiFe-OH-PO<sub>4</sub>/NF. At the same overpotential, only 251 and 62 mA cm<sup>-2</sup> could be obtained for NiFe-OH/NF and RuO<sub>2</sub>/NF electrodes, respectively.

The Tafel slopes for all of the electrodes were investigated to further understand their OER activities (Figure 3b). The Tafel slope of NiFe-OH-PO<sub>4</sub>/NF (41.76 mV dec<sup>-1</sup>) is much smaller than that of NiFe-OH/NF (55.75 mV dec<sup>-1</sup>), RuO<sub>2</sub>/NF (83.50 mV dec<sup>-1</sup>), and NF (118.24 mV dec<sup>-1</sup>), and is also the lowest compared with that of the recently reported bifunctional electrocatalysts for OER, such as CoP film (47 mV dec<sup>-1</sup>),<sup>46</sup> P/CTs/Co-S (72 mV dec<sup>-1</sup>),<sup>47</sup> NiMo HNRs/TiM (47 mV

dec<sup>-1</sup>),<sup>48</sup> and Ni<sub>0.9</sub>Fe<sub>0.1</sub>/NC (45 mV dec<sup>-1</sup>)<sup>49</sup> (Table S1). The small Tafel slope means fast OER kinetics and excellent charge transfer properties of the NiFe-OH-PO<sub>4</sub>/NF catalyst. Then, the intrinsic OER catalytic activity of NiFe-OH-PO<sub>4</sub>/NF is further evaluated by calculating the turnover frequency (TOF) by assuming that all of the Ni sites are involved in OER. The TOF for NiFe-OH-PO<sub>4</sub> at the overpotential of 400 mV is 0.227 s<sup>-1</sup>, which is also among the highest in the state-of-the-art OER electrocatalysts.<sup>9,27</sup>

The stability of the NiFe-OH-PO<sub>4</sub>/NF catalyst is investigated by multistep chronopotentiometric responses, and the results are displayed in Figure 3c. When the current densities are increased from 50 to 550 mA cm<sup>-2</sup> with an increment of 100 mA cm<sup>-2</sup> per 1000 s, the polarization potential increases immediately and then levels off to remain constant for the rest 1000 s for all of the current densities up to 550 mA cm<sup>-2</sup>. Moreover, the almost same potential value is established at the same current density for the reverse process. The results indicate that NiFe-OH-PO<sub>4</sub>/NF electrode has excellent mass transport properties, conductivity, and mechanical robustness. The continuous and long-term robustness of the NiFe-OH-PO<sub>4</sub>/NF electrode at the current densities of 100 and 500 mA cm<sup>-2</sup> in both 1.0 M KOH and in a 30% KOH solution were also investigated (Figures 3d, S7 and S8). The results indicate the NiFe-OH-PO<sub>4</sub>/NF electrode remains stable with no detectable current decay during the course of testing. These results suggest the performance NiFe-OH-PO<sub>4</sub>/NF electrode can faithfully satisfy the industrial requirements.

**Hydrogen Evolution Activity.** The catalytic activities of the NiFe-OH-PO<sub>4</sub>/NF, NiFe-OH/NF, NF, and Pt/C/NF electrodes for HER in the same electrolyte are also assessed, and the results are shown in Figure 4a. Despite the excellent

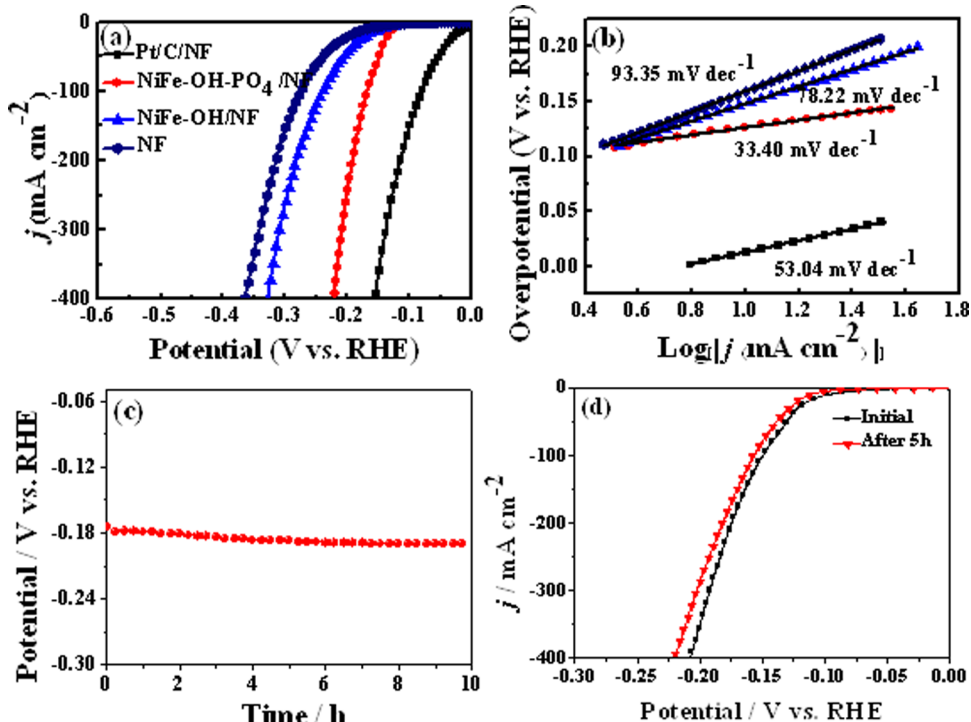


**Figure 4.** (a) HER polarization curves for Pt/C/NF, NiFe-OH-PO<sub>4</sub>/NF, NiFe-OH/NF, and NF electrodes at 2.0 mV s<sup>-1</sup> with *iR* compensations. (b) The corresponding Tafel plots. (c) Chronopotentiometric curve of NiFe-OH-PO<sub>4</sub>/NF with constant current density of 50 mA cm<sup>-2</sup>. (d) HER polarization curves recorded NiFe-OH-PO<sub>4</sub>/NF catalyzing water with constant current density of 50 mA cm<sup>-2</sup> initial and after 5 h.

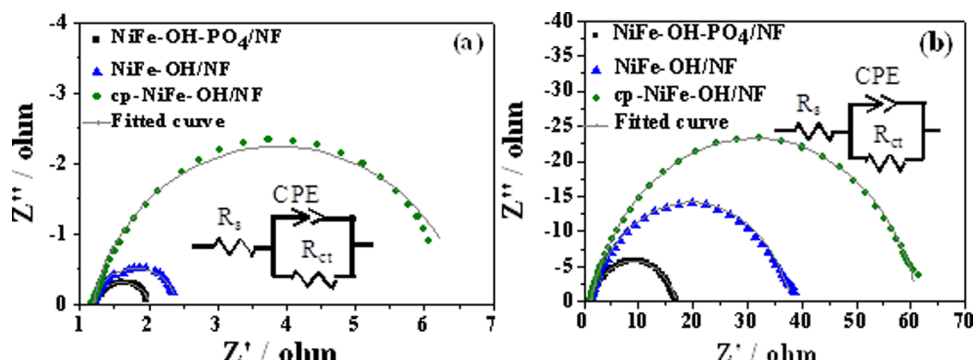


**Figure 5.** (a) Nyquist plots obtained by EIS at 300 mV overpotential for the OER. (b) Nyquist plots obtained by EIS at 150 mV overpotential for HER.

OER performance achieved for NiFe-OH/NF, the HER activity gained was poor. In contrast, the NiFe-OH-PO<sub>4</sub>/NF electrode shows a high HER activity, which requires only an overpotential  $\eta = 135$  mV to reach the current density of 20 mA cm<sup>-2</sup>. This performance is lower than that of the Pt/C/NF electrode ( $\eta = 30.2$  mV) but superior to the state-of-the-art nonprecious HER electrocatalysts reported at even lower current density of 10 mA cm<sup>-2</sup>, such as CoO<sub>x</sub>@CN (134 mV),<sup>40</sup> NiFe-LDH/NF (250 mV),<sup>41</sup> Ni<sub>3</sub>S<sub>2</sub> /NF (223 mV),<sup>39</sup> CoP-MNA (74 mV),<sup>43</sup> and Co@N-C (108 mV).<sup>50</sup> A detailed comparison of NiFe-OH-PO<sub>4</sub>/NF with other highly active HER electrocatalyst is shown in Table S1. In addition, the fast HER kinetics at NiFe-OH-PO<sub>4</sub>/NF is revealed by an extremely small Tafel plot of 33.4 mV dec<sup>-1</sup> (Figure 4b), which is among the smallest Tafel value of reported HER catalysts in the alkaline media (Table S1). The NiFe-OH-PO<sub>4</sub>/NF electrode also shows excellent stability in a long-term HER in 1.0 M KOH (Figure 4c,d).

To understand the extraordinary performance of the NiFe-OH-PO<sub>4</sub>/NF electrode for both OER and HER, the electrochemical surface areas (ECSA) of NiFe-OH-PO<sub>4</sub>/NF electrode and NF electrode were measured by determining their double-layer capacitance ( $C_{DL}$ ) using cyclic voltammetry (Figures S9 and S10, Table S2).<sup>50–52</sup> The ECSA of NiFe-OH-PO<sub>4</sub>/NF electrode is 41.8 cm<sup>2</sup>, much higher than the ECSA of 34.2 cm<sup>2</sup> of NF electrode. In addition, SEM study (Figure 1c) shows that the nanobelts are tightly attached to the NF support, offering excellent ohmic contacts and low resistance, which can be also confirmed by electrochemical impedance spectroscopy (EIS). As shown in Figure 5, the electrocatalytic kinetics of charge transfer was determined by measuring the charge transfer resistance ( $R_{ct}$ ). The  $R_{ct}$  values of NiFe-OH-PO<sub>4</sub>/NF for OER and HER processes are 0.8 and 15.7 Ω cm<sup>-2</sup> (Table S3), respectively, which are much smaller than those of NiFe-OH/NF (1.24 and 36.9 Ω cm<sup>-2</sup>) and cp-NiFe-OH/NF (5.4 and 60.4 Ω cm<sup>-2</sup>). The variation tendency of the  $R_{ct}$  is consistent

with the linear sweep voltammetry results, indicating a small  $R_{ct}$  value and faster electrode kinetics.

**Overall Water Splitting.** Figure 6 shows the overall water electrolysis polarization curves of NiFe-OH-PO<sub>4</sub>/NF and cp-

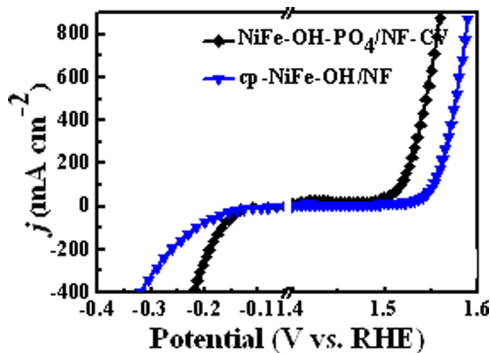


**Figure 6.** Overall water electrolysis polarization curves of NiFe-OH-PO<sub>4</sub>/NF and cp-NiFe-OH/NF electrodes in 1.0 M KOH at 2.0 mV s<sup>-1</sup> with *iR* compensations.

NiFe-OH/NF electrodes in 1.0 M KOH. The electrocatalytic activities of NiFe-OH-PO<sub>4</sub>/NF electrode for OER and HER are much higher than those of cp-NiFe-OH/NF, suggesting a strong synergistic effect upon phosphorylation of NiFe hydroxides. It is hypothesized that phosphate groups enhances OER and HER via different mechanisms. For OER, the distorted geometry of nickel or iron with open coordinate sites caused by the phosphate groups can enhance the catalytic activity sites and favors OH<sup>-</sup> adsorption.<sup>53–55</sup> For HER, the

improvement in electrocatalytic activity can be attributed to the formation of phosphides by in situ reduction of phosphate groups during HER processes.

After the water-splitting experiments, the surface morphology and component analysis of NiFe-OH-PO<sub>4</sub>/NF electrodes were characterized by SEM, XRD, and XPS again. The surface morphology of NiFe-OH-PO<sub>4</sub>/NF composites changed less after the OER and HER process (Figure S11), and the NiFe-OH-PO<sub>4</sub> composites also retained the amorphous structures (Figure S12). However, the XPS spectra of NiFe-OH-PO<sub>4</sub>/NF after the OER and HER processes showed different results. After OER, the chemical states of all of the elements in NiFe-OH-PO<sub>4</sub> composites were same as those of the original sample (Figure S13). But after the HER process, the peak at ~133.2 eV ascribed to phosphate group disappeared in the high-resolution P 2p XPS spectrum and a new peak at 132.5 eV, which is attributed to the formation of phosphides, appeared (Figure S13).

On the basis of the polarization curves above, it is anticipated that the NiFe-OH-PO<sub>4</sub>/NF electrode can serve as a bifunctional electrocatalyst for overall water splitting. Therefore, a two-electrode electrolyzer using the NiFe-OH-PO<sub>4</sub>/NF electrode as both the anode and the cathode (NiFe-OH-PO<sub>4</sub>/NF||NiFe-OH-PO<sub>4</sub>/NF) is demonstrated. For comparison purpose, a control electrolyzer using the benchmark RuO<sub>2</sub>/NF as the anode and Pt/C/NF as the cathode (RuO<sub>2</sub>/NF||Pt/C/NF) is also examined under the same condition. Figure 7a shows the OER polarization curves for both electrolyzers. Though NiFe-OH-PO<sub>4</sub>/NF||NiFe-OH-PO<sub>4</sub>/NF system exhibits a slightly larger onset potential, its current density increases

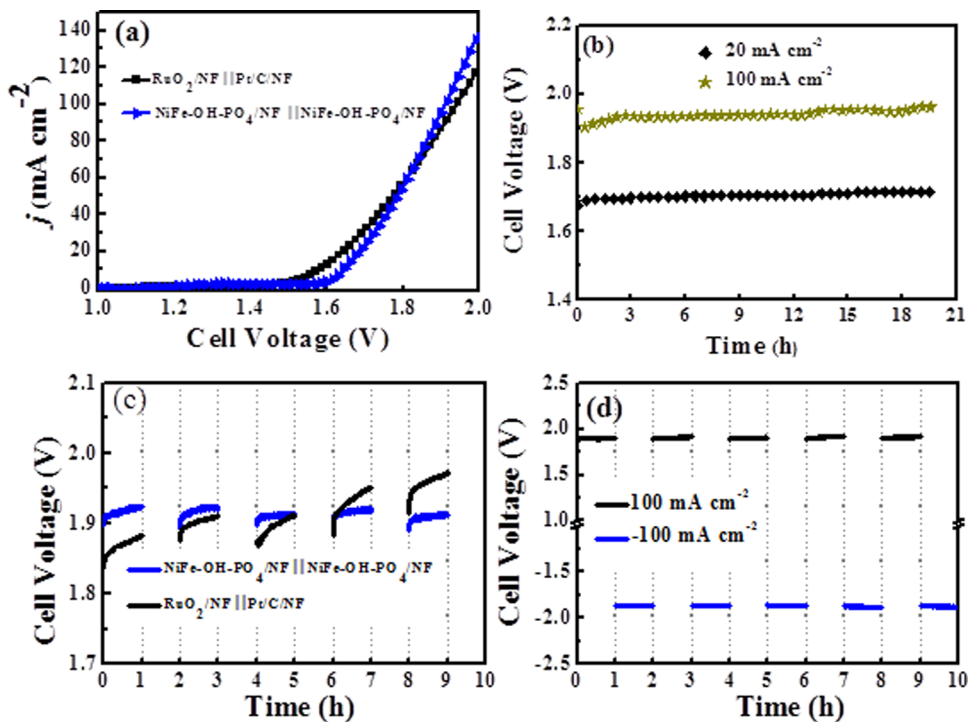


**Figure 7.** Water electrolysis performance obtained in the two-electrode system employing NiFe-OH-PO<sub>4</sub>/NF as both the anode and cathode in 1.0 M KOH. (a) OER polarization curves for RuO<sub>2</sub>/NF||Pt/C/NF and NiFe-OH-PO<sub>4</sub>/NF||NiFe-OH-PO<sub>4</sub>/NF at 2.0 mV s<sup>-1</sup> without *iR* compensations. (b) Chronoamperometric curves with constant current density of 20 and 100 mA cm<sup>-2</sup>. (c) Galvanostatic curves obtained with the RuO<sub>2</sub>/NF||Pt/C/NF and NiFe-OH-PO<sub>4</sub>/NF||NiFe-OH-PO<sub>4</sub>/NF anode and cathode during power interruptions. The applied current density is 100 mA cm<sup>-2</sup>, and the periods for continuous electrolysis and power shutdowns are 1 h. (d) Galvanostatic curves obtained with NiFe-OH-PO<sub>4</sub>/NF as both the anode and cathode. The applied current density is 100 mA cm<sup>-2</sup>, and the polarity of electrode is reversed every 1 h.

much faster than that of the commercial RuO<sub>2</sub>/NF||Pt/C/NF system at higher potentials due to the smaller Tafel slopes and faster reaction kinetics of NiFe-OH-PO<sub>4</sub>/NF for OER and HER. Figure 7b further shows the long-period stability of the NiFe-OH-PO<sub>4</sub>/NF||NiFe-OH-PO<sub>4</sub>/NF electrolyzer at the current densities of 20 and 100 mA cm<sup>-2</sup> for 20 h. Stable cell potentials of 1.68 and 1.91 V was obtained without a noticeable decay, respectively. The water-splitting voltage at the current density of 10 mA cm<sup>-2</sup> is lower than that of the state-of-the-art nonprecious bifunctional catalysts reported recently (Table S4).

The stability of the NiFe-OH-PO<sub>4</sub>/NF electrodes is further tested under frequent cell shutdowns to mimic the intermittent industrial electrolysis operation conditions. Figure 7c displays the galvanostatic curves tested under an applied current density of 100 mA cm<sup>-2</sup> for five consequent shutdown/start-up cycles with a shutdown interval of 1 h. For the NiFe-OH-PO<sub>4</sub>/NF||/NiFe-OH-PO<sub>4</sub>/NF system, the cell voltage remains stable at 1.91 V after each power shutdown. In contrast, the RuO<sub>2</sub>/NF||Pt/C/NF system shows a gradual deterioration after each cycle of shutdown/start-up, and ~100 mV increase in the cell voltages after five cycles indicates its poor stability under intermittent water electrolysis.

Finally, the robustness of the NiFe-OH-PO<sub>4</sub>/NF electrode is demonstrated under even more harsh conditions by alternating the polarity of the electrode repeatedly. In this experiment, the polarity of the two NiFe-OH-PO<sub>4</sub>/NF electrodes in the cell is reversed every hour, and the NiFe-OH-PO<sub>4</sub>/NF electrode is subjected to anodic oxidation for OER for an hour before switching to HER. As seen from Figure 7d, when NiFe-OH-PO<sub>4</sub>/NF is used as the anode at a current density of 100 mA cm<sup>-2</sup> for OER, the cell voltage is stabilized at 1.91 V. Remarkably, when the electrode polarity is changed to HER, the cell voltage is maintained at -1.91 V, and no increase in the cell voltage is observed after reversing the electrode polarity for nine cycles. The above results suggest the as-prepared NiFe-OH-PO<sub>4</sub>/NF electrode is fully reversible, interexchangeable between OER and HER, and extremely robust for intermittent water electrolysis. These properties can significantly improve the robustness and simplification of the water-splitting system and lower the manufacturing cost for hydrogen production.

## CONCLUSIONS

A 3D NiFe-OH-PO<sub>4</sub>/NF electrocatalyst with well-controlled hierarchical porous structure, composition, and catalytic activity is prepared via a facile cyclic voltammetry deposition method. The electrodeposited NiFe hydroxides on the cathodic scan are subsequently phosphorylated on the anodic sweeps to form NiFe hydroxyphosphate. The prepared porous electrode shows not only significantly enhanced synergistic catalytic activities toward both OER and HER but also remarkable stability for the whole-cell water splitting under continuous and intermittent electrolysis conditions. It is anticipated that the cyclic voltammetry approach can be applied for the controlled phosphorylation of a range of electrodeposited electrocatalysts for achieving enhanced catalytic performance. The excellent catalytic activity, stability, and the facile and scale-up fabrication process of the NiFe hydroxyphosphate catalyst make it promising for use as a noble-metal-free water-splitting electrode for industrial water electrolysis.

## ASSOCIATED CONTENT

### Supporting Information

The Supporting Information is available free of charge on the ACS Publications website at DOI: 10.1021/acsami.7b10385.

SEM, energy-dispersive X-ray, XRD, XPS images, and Raman spectroscopy of NiFe-OH-PO<sub>4</sub>/NF composite; SEM, XRD, and XPS images of NiFe-OH-PO<sub>4</sub>/NF composite after the water-splitting experiments; electrochemical characterization of NiFe-OH-PO<sub>4</sub>/NF electrode for HER and OER; cyclic voltammograms of NiFe-OH-PO<sub>4</sub>/NF and NF electrodes for the measurement of the electrochemically active surface areas (ECAS) (PDF)

## AUTHOR INFORMATION

### Corresponding Authors

\*E-mail: wangzl@snnu.edu.cn (Z.W.).

\*E-mail: chuan.zhao@unsw.edu.au. Fax: (0086)-29-81530727 (C.Z.).

### ORCID

Yibing Li: 0000-0002-1729-5963

Zenglin Wang: 0000-0002-4903-5621

Chuan Zhao: 0000-0001-7007-5946

### Notes

The authors declare no competing financial interest.

## ACKNOWLEDGMENTS

The project was financially supported by National Natural Science Foundation of China (No. 21273144), the 111 Project (No. B14041), Program for Chang Jiang Scholars and Innovative Research Team in University (IRT-14R33), and an Australian Research Council Discovery Grant (DP160103107).

## REFERENCES

- (1) Turner, J. A. Sustainable Hydrogen Production. *Science* **2004**, *305*, 972–974.
- (2) Dresselhaus, M. S.; Thomas, I. L. Alternative energy technologies. *Nature* **2001**, *414*, 332–337.
- (3) Tang, C.; Cheng, N.; Pu, Z.; Xing, W.; Sun, X. NiSe Nanowire Film Supported on Nickel Foam: An Efficient and Stable 3D Bifunctional Electrode for Full Water Splitting. *Angew. Chem.* **2015**, *127*, 9483–9487.
- (4) Walter, M. G.; Warren, E. L.; McKone, J. R.; Boettcher, S. W.; Mi, Q.; Santori, E. A.; Lewis, N. S. Solar Water Splitting Cells. *Chem. Rev.* **2010**, *110*, 6446–6473.
- (5) Carmo, M.; Fritz, D. L.; Merge, J.; Stolten, D. A Comprehensive Review on PEM Water Electrolysis. *Int. J. Hydrogen Energy* **2013**, *38*, 4901–4934.
- (6) Reier, T.; Pawolek, Z.; Cherevko, S.; Bruns, M.; Jones, T.; Teschner, D.; Selve, S.; Bergmann, A.; Nong, H. N.; Schlogl, R.; Mayrhofer, K. J. J.; Strasser, P. Molecular Insight in Structure and Activity of Highly Efficient, Low-Ir Ir-Ni Oxide Catalysts for Electrochemical Water Splitting (OER). *J. Am. Chem. Soc.* **2015**, *137*, 13031–13040.
- (7) McCrory, C. C. L.; Jung, S. H.; Ferrer, I. M.; Chatman, S. M.; Peters, J. C.; Jaramillo, T. F. Benchmarking Hydrogen Evolving Reaction and Oxygen Evolving Reaction Electrocatalysts for Solar Water Splitting Devices. *J. Am. Chem. Soc.* **2015**, *137*, 4347–4357.
- (8) Smith, R. D. L.; Prévôt, M. S.; Fagan, R. D.; Zhang, Z. P.; Sedach, P. A.; Siu, M. K. J.; Trudel, S.; Berlinguette, C. P. Photochemical Route for Accessing Amorphous Metal Oxide Materials for Water Oxidation Catalysis. *Science* **2013**, *340*, 60–63.
- (9) Gao, M.; Sheng, W.; Zhuang, Z.; Fang, Q.; Gu, S.; Jiang, J.; Yan, Y. Efficient Water Oxidation Using Nanostructured  $\alpha$ -Nickel-

- Hydroxide As an Electrocatalyst. *J. Am. Chem. Soc.* **2014**, *136*, 7077–7084.
- (10) Kanan, M. W.; Nocera, D. G. In Situ Formation of an Oxygen-Evolving Catalyst in Neutral Water Containing Phosphate and  $\text{Co}^{2+}$ . *Science* **2008**, *321*, 1072–1075.
- (11) Cheng, N. Y.; Liu, Q.; Asiri, A. M.; Xing, W. X.; Sun, P. A Fe-doped  $\text{Ni}_3\text{S}_2$  Particle Film As a High-efficiency Robust Oxygen Evolution Electrode with Very High Current Density. *J. Mater. Chem. A* **2015**, *3*, 23207–23212.
- (12) Trotochaud, L.; Young, S. L.; Ranney, J. K.; Boettcher, S. W. Nickel-Iron Oxyhydroxide Oxygen-Evolution Electrocatalysts: The Role of Intentional and Incidental Iron Incorporation. *J. Am. Chem. Soc.* **2014**, *136*, 6744–6753.
- (13) Xu, K.; Chen, P. Z.; Li, X. L.; Tong, Y.; Ding, H.; Wu, X. J.; Chu, W. S.; Peng, Z. M.; Wu, C. Z.; Xie, Y. Metallic Nickel Nitride Nanosheets Realizing Enhanced Electrochemical Water Oxidation. *J. Am. Chem. Soc.* **2015**, *137*, 4119–4125.
- (14) Tan, Y. W.; Wang, H.; Liu, P.; Shen, Y. H.; Cheng, C.; Hirata, A.; Fujita, T.; Tang, Z.; Chen, M. W. Versatile Nanoporous Bimetallic Phosphides Towards Electrochemical Water Splitting. *Energy Environ. Sci.* **2016**, *9*, 2257–2261.
- (15) Tian, J.; Liu, Q.; Asiri, A. M.; Sun, X. Self-Supported Nanoporous Cobalt Phosphide Nanowire Arrays: An Efficient 3D Hydrogen-Evolving Cathode over the Wide Range of pH 0–14. *J. Am. Chem. Soc.* **2014**, *136*, 7587–7590.
- (16) Meyer, S.; Nikiforov, A. V.; Petrushina, I. M.; Kohler, K.; Christensen, E.; Jensen, J. O.; Bjerrum, N. J. Transition Metal Carbides ( $\text{WC}$ ,  $\text{Mo}_2\text{C}$ ,  $\text{TaC}$ ,  $\text{NbC}$ ) as Potential Electrocatalysts for the Hydrogen Evolution Reaction (HER) at Medium Temperatures. *Int. J. Hydrogen Energy* **2015**, *40*, 2905–2911.
- (17) Gong, M.; Zhou, W.; Tsai, M. C.; Zhou, J. G.; Guan, M. Y.; Lin, M. C.; Zhang, B.; Hu, Y. F.; Wang, D. Y.; Yang, J.; Pennycook, S. J.; Hwang, B. J.; Dai, H. J. Nanoscale Nickel Oxide/nickel Heterostructures for Active Hydrogen Evolution Electrocatalysis. *Nat. Commun.* **2014**, *5*, No. 4695.
- (18) Long, X.; Li, G. X.; Wang, Z. L.; Zhu, H. Y.; Zhang, T.; Xiao, S.; Guo, W. Y.; Yang, S. H. Metallic Iron-Nickel Sulfide Ultrathin Nanosheets As a Highly Active Electrocatalyst for Hydrogen Evolution Reaction in Acidic Media. *J. Am. Chem. Soc.* **2015**, *137*, 11900–11903.
- (19) Schäfer, H.; Sadaf, S.; Walder, L.; Kuepper, K.; Dinklage, S.; Wollschläger, J.; Schneider, L.; Steinhart, M.; Hardege, J.; Daum, D. Stainless Steel Made to Rust: a Robust Water-splitting Catalyst with Benchmark Characteristics. *Energy Environ. Sci.* **2015**, *8*, 2685–2697.
- (20) Schäfer, H.; Chevrier, D. M.; Kuepper, K.; Zhang, P.; Wollschlaeger, J.; Daum, D.; Steinhart, M.; He, C.; Krupp, U.; Müller-Buschbaum, K.; Stangl, J.; Schmidt, M.  $\text{X}_{20}\text{CoCrWMo}_{10.9}/\text{Co}_3\text{O}_4$ : a Metal–Ceramic Composite with Unique Efficiency Values for Water-Splitting in the Neutral Regime. *Energy Environ. Sci.* **2016**, *9*, 2609–2622.
- (21) Yu, F.; Li, F.; Sun, L. Stainless Steel as an Efficient Electrocatalyst for Water Oxidation in Alkaline Solution. *Int. J. Hydrogen Energy* **2016**, *41*, 5230–5233.
- (22) Tang, D.; Mabayoje, O.; Lai, Y.; Liu, Y.; Mullins, C. B. In Situ Growth of  $\text{Fe}(\text{Ni})\text{OOH}$  Catalyst on Stainless Steel for Water Oxidation. *ChemistrySelect* **2017**, *2*, 2230–2234.
- (23) Schäfer, H.; Beladi-Mousavi, S. M.; Walder, L.; Wollschläger, J.; Kuschel, O.; Ichilmann, S.; Sadaf, S.; Steinhart, M.; Kupper, K.; Schneider, L. Surface Oxidation of Stainless Steel: Oxygen Evolution Electrocatalysts with High Catalytic Activity. *ACS Catal.* **2015**, *5*, 2671–2680.
- (24) Schäfer, H.; Chevrier, D. M.; Zhang, P.; Stangl, J.; Müller-Buschbaum, K.; Hardege, J. D.; Kuepper, K.; Wollschläger, J.; Krupp, U.; Dühnen, S.; Steinhart, M.; Walder, L.; Sadaf, S.; Schmidt, M. Electro-Oxidation of  $\text{Ni}_{42}$  Steel: A Highly Active Bifunctional Electrocatalyst. *Adv. Funct. Mater.* **2016**, *26*, 6402–6417.
- (25) Song, F.; Hu, X. L. Exfoliation of Layered Double Hydroxides for Enhanced Oxygen Evolution Catalysis. *Nat. Commun.* **2014**, *5*, No. 4477.
- (26) Gong, M.; Dai, H. J. A Mini Review of NiFe-based Materials as Highly Active Oxygen Evolution Reaction Electrocatalysts. *Nano Res.* **2015**, *8*, 23–39.
- (27) Lu, X.; Zhao, C. Electrodeposition of Hierarchically Structured Three-dimensional Nickel-iron Electrodes for Efficient Oxygen Evolution at High Current Densities. *Nat. Commun.* **2015**, *6*, No. 6616.
- (28) Cobo, S.; Heidkamp, J.; Jacques, P. A.; Fize, J.; Fourmond, V.; Guetaz, L.; Jousselme, B.; Ivanova, V.; Dau, H.; Palacin, S.; Fontecave, M.; Artero, V. A Janus Cobalt-based Catalytic Material for Electro-splitting of Water. *Nat. Mater.* **2012**, *11*, 802–807.
- (29) Xing, J.; Li, H.; Cheng, M. M. C.; Geyer, S. M.; Ng, K. Y. S. Electro-synthesis of 3D Porous Hierarchical Ni–Fe Phosphate Film/Ni Foam as a High-efficiency Bifunctional Electrocatalyst for Overall Water Splitting. *J. Mater. Chem. A* **2016**, *4*, 13866–13873.
- (30) Augustyn, V.; Therese, S.; Turner, T. C.; Manthiram, A. Nickel-rich Layered  $\text{LiNi}_{1-x}\text{M}_x\text{O}_2$  ( $\text{M} = \text{Mn}, \text{Fe}$ , and  $\text{Co}$ ) Electrocatalysts with High Oxygen Evolution Reaction Activity. *J. Mater. Chem. A* **2015**, *3*, 16604–16612.
- (31) Lopez, M. C.; Ortiz, G. F.; Lavela, P.; Alcantara, R.; Tirado, J. L. Improved Energy Storage Solution Based on Hybrid Oxide Materials. *ACS Sustainable Chem. Eng.* **2013**, *1*, 46–56.
- (32) Zhou, W. J.; Wu, X. J.; Cao, X. H.; Huang, X.; Tan, C. L.; Tian, J.; Liu, H.; Wang, J. Y.; Zhang, H.  $\text{Ni}_3\text{S}_2$  Nanorods/Ni foam Composite Electrode with Low Overpotential for Electrocatalytic Oxygen Evolution. *Energy Environ. Sci.* **2013**, *6*, 2921–2924.
- (33) Kim, K. H.; Zheng, J. Y.; Shin, W.; Kang, Y. S. Preparation of Dendritic NiFe Films by Electrodeposition for Oxygen evolution. *RSC Adv.* **2012**, *2*, 4759–4767.
- (34) Peng, C. Y.; Kang, L.; Cao, S.; Chen, Y.; Lin, Z. S.; Fu, W. F. Nanostructured  $\text{Ni}_2\text{P}$  As a Robust Catalyst for the Hydrolytic Dehydrogenation of Ammonia-Borane. *Angew. Chem., Int. Ed.* **2015**, *54*, 15725–15729.
- (35) Chemelewski, W. D.; Lee, H. C.; Lin, J. F.; Bard, A. J.; Mullins, C. B. Amorphous FeOOH Oxygen Evolution Reaction Catalyst for Photoelectrochemical Water Splitting. *J. Am. Chem. Soc.* **2014**, *136*, 2843–2850.
- (36) Chen, G.; Zhao, Y.; Fu, G.; Duchesne, P. N.; Gu, L.; Zheng, Y. P.; Weng, X. F.; Chen, M. S.; Zhang, P.; Pao, C. W.; Lee, J. F.; Zheng, N. F. Interfacial Effects in Iron-Nickel Hydroxide-Platinum Nanoparticles Enhance Catalytic Oxidation. *Science* **2014**, *344*, 495–499.
- (37) Landon, J.; Demeter, E.; Inoglu, N.; Keturakis, C.; Wachs, I. E.; Vasić, R.; Frenkel, A. I.; Kitchin, J. R. Spectroscopic Characterization of Mixed Fe-Ni Oxide Electrocatalysts for the Oxygen Evolution Reaction in Alkaline Electrolytes. *ACS Catal.* **2012**, *2*, 1793–1801.
- (38) Yan, J.; Fan, Z.; Sun, W.; Ning, G.; Wei, T.; Zhang, Q.; Zhang, R.; Zhi, L.; Wei, F. Advanced Asymmetric Supercapacitors Based on  $\text{Ni(OH)}_2/\text{graphene}$  and Porous Graphene Electrodes with High Energy Density. *Adv. Funct. Mater.* **2012**, *22*, 2632–2641.
- (39) Hu, H.; Xiao, W. J.; Yuan, J.; Shi, J. W.; He, D. N.; Shangguan, W. F. High Photocatalytic Activity and Stability for Decomposition of Gaseous Acetaldehyde on  $\text{TiO}_2/\text{Al}_2\text{O}_3$  Composite Films Coated on Foam Nickel Substrates by Sol-gel Processes. *J. Sol-Gel Sci. Technol.* **2008**, *45*, 1–8.
- (40) Jin, H. Y.; Wang, J.; Su, D. F.; Wei, Z. Z.; Pang, Z. F.; Wang, Y. In-situ Cobalt-cobalt oxide/N-doped Carbon Hybrids As Superior Bi-functional Electrocatalysts for Hydrogen and Oxygen Evolution. *J. Am. Chem. Soc.* **2015**, *137*, 2688–2694.
- (41) Luo, J.; Im, J. H.; Mayer, M. T.; Schreier, M.; Nazeeruddin, M. K.; Park, N. G.; Tilley, S. D.; Fan, H.; Grätzel, M. Water Photolysis at 12.3% Efficiency via Perovskite Photovoltaics and Earth-abundant Catalysts. *Science* **2014**, *345*, 1593–1596.
- (42) Feng, L. L.; Yu, G. T.; Wu, Y. Y.; Li, G. D.; Li, H.; Sun, Y. H.; Asefa, T.; Chen, W.; Zou, X. X. High-index Faceted  $\text{Ni}_3\text{S}_2$  Nanosheet Arrays As Highly Active and Ultrastable Electrocatalysts for Water Splitting. *J. Am. Chem. Soc.* **2015**, *137*, 14023–14026.
- (43) Zhu, Y. P.; Liu, Y. P.; Ren, T. Z.; Yuan, Z. Y. Self-Supported Cobalt Phosphide Mesoporous Nanorod Arrays: A Flexible and

- Bifunctional Electrode for Highly Active Electrocatalytic Water Reduction and Oxidation. *Adv. Funct. Mater.* **2015**, *25*, 7337–7347.
- (44) Yang, Y.; Fei, H. L.; Ruan, G. D.; Tour, J. M. Porous Cobalt-Based Thin Film As a Bifunctional Catalyst for Hydrogen Generation and Oxygen Generation. *Adv. Mater.* **2015**, *27*, 3175–3180.
- (45) Ledendecker, M.; Calderýn, S. K.; Papp, C.; Steinrück, H.-P.; Antonietti, M.; Shalom, M. The Synthesis of Nanostructured Ni<sub>3</sub>P<sub>4</sub> Films and their Use As a Non-Noble Bifunctional Electrocatalyst for Full Water Splitting. *Angew. Chem.* **2015**, *127*, 12538–12542.
- (46) Jiang, N.; You, B.; Sheng, M. L.; Sun, Y. J. Electrodeposited Cobalt- Phosphorous-Derived Films As Competent Bifunctional Catalysts for Overall Water Splitting. *Angew. Chem.* **2015**, *127*, 6349–6352.
- (47) Wang, J.; Zhong, H. X.; Wang, Z. L.; Meng, F. L.; Zhang, X. B. Integrated Three-Dimensional Carbon Paper/Carbon Tubes/Cobalt-Sulfide Sheets As An Efficient Electrode for Overall Water Splitting. *ACS Nano* **2016**, *10*, 2342–2348.
- (48) Tian, J. Q.; Cheng, N.; Liu, Y. Q.; Sun, X. P.; He, Y. Q.; Asiri, A. M. Self-supported NiMo Hollow Nanorod Array: An Efficient 3D Bifunctional Catalytic Electrode for Overall Water Splitting. *J. Mater. Chem. A* **2015**, *3*, 20056–20059.
- (49) Zhang, X.; Xu, H. M.; Li, X. X.; Li, Y. Y.; Yang, T. B.; Liang, Y. Y. Facile Synthesis of Nickel-Iron/Nanocarbon Hybrids As Advanced Electrocatalysts for Efficient Water Splitting. *ACS Catal.* **2016**, *6*, 580–588.
- (50) Benck, J. D.; Chen, Z. B.; Kuritzky, L. Y.; Forman, A. J.; Jaramillo, T. F. Amorphous Molybdenum Sulfide Catalysts for Electrochemical Hydrogen Production: Insights into the Origin of their Catalytic Activity. *ACS Catal.* **2012**, *2*, 1916–1923.
- (51) McCrory, C. C. L.; Jung, S.; Peters, J. C.; Jaramillo, T. F. Benchmarking Heterogeneous Electrocatalysts for the Oxygen Evolution Reaction. *J. Am. Chem. Soc.* **2013**, *135*, 16977–16987.
- (52) Lu, X.; Yim, W.-L.; Suryanto, B. H. R.; Zhao, C. Electrocatalytic Oxygen Evolution at Surface-Oxidized Multiwall Carbon Nanotubes. *J. Am. Chem. Soc.* **2015**, *137*, 2901–2907.
- (53) Liu, Y.; Cheng, H.; Lyu, M.; Fan, S.; Liu, Q.; Zhang, W.; Zhi, Y.; Wang, C.; Xiao, C.; Wei, S.; Ye, B.; Xie, Y. Low Overpotential in Vacancies-Rich Ultrathin CoSe<sub>2</sub> Nanosheets for Water Oxidation. *J. Am. Chem. Soc.* **2014**, *136*, 15670–15675.
- (54) Kim, J.; Yin, X.; Tsao, K. C.; Fang, S.; Yang, H. Ca<sub>2</sub>Mn<sub>2</sub>O<sub>5</sub> As Oxygen-deficient Perovskite Electrocatalyst for Oxygen Evolution Reaction. *J. Am. Chem. Soc.* **2014**, *136*, 14646–14649.
- (55) Kim, H.; Park, J.; Park, I.; Jin, K.; Jeng, S. E.; Kim, S. H.; Nam, K. T.; Kang, K. Coordination Tuning of Cobalt Phosphates Towards Efficient Water Oxidation Catalyst. *Nat. Commun.* **2015**, *6*, No. 8253.